Geophysical Journal International

Geophys. J. Int. (2023) **232,** 81–96
Advance Access publication 2022 August 23
GJI Seismology

https://doi.org/10.1093/gji/ggac327

Decoding the Emeishan Permian mantle plume in the southeastern margin of Tibet from the seismic signature of the local lithosphere

Jiafu Hu,[1] Haiyan Yang,[1] José Badal,[2] Hengchu Peng[1] and Suqiu Miao[1]

[1] *Department of Geophysics, Yunnan University,* 2 *North Green Lake Rd., Kunming, Yunnan* 650091, *P.R. China. E-mail: jfhu96@163.com*
[2] *Physics of the Earth, Sciences B, University of Zaragoza, Pedro Cerbuna* 12, 50009 *Zaragoza, Spain*

Accepted 2022 August 15. Received 2022 August 10; in original form 2022 January 24

SUMMARY

The Emeishan large igneous province (ELIP), which is located along the southeastern margin of Tibet, is widely regarded as the erosional remnants of voluminous Permian mafic volcanic successions that were associated with mantle plume activity. In addition, evidence for the eruption of the mantle plume and its signature of lithospheric modification should have been retained in the lithosphere after cooling of the plume. Here we use calculated compressional- and shear wave receiver functions (PRFs and SRFs, respectively) from >750 broad-band stations, together with heat flow and Bouguer gravity anomaly data, to investigate the seismic signature within the lithosphere beneath the southeastern margin of Tibet. Our results from the inner zone (INZ) of the ELIP indicate that the ∼60 km depth of the Moho interpreted from depth-migrated PRF images is consistent with that inferred from SRFs and is deeper than that in the region surrounding the INZ, which shows a continuous positive converted phase at ∼35–40 km depth. The crustal geometry and physical properties show a 15–20-km-thick mafic underplated layer that extends for 150–200 km in the E–W direction and ∼400 km in the N–S direction along the base of the crust in the northeastern INZ and its surrounding region. We interpret the underplated layer as the concealed Emeishan plume hotspot track and suggest that the head of the postulated mantle plume is centred approximately beneath Panzhihua City and its surroundings. We propose a new geodynamic model for the formation of the ELIP, in which the lower–middle crust has been strengthened by voluminous mafic intrusions and underplating, whereas the Yangtze Craton in the plume region has been destroyed by removing the base of the lithosphere.

Key words: Heat flow; Gravity anomalies and Earth structure; Crustal imaging; Interface waves; Dynamics of lithosphere and mantle; Large igneous provinces.

1 INTRODUCTION

Global positioning system (GPS) velocity vectors have indicated that the upper crust along the southeastern margin of Tibet is undergoing clockwise rotation around the Eastern Himalayan Syntax (EHS; Zhang *et al.* 2004). The left-lateral Xianshuihe-Xiaojiang fault (F9 and F6 in Fig. 1) and the right-lateral Jinshajiang-Red River fault (F7 in Fig. 1) separate the southeastern margin of Tibet into different tectonic blocks, such as Indochina Block and the Sichuan–Yunnan diamond-shaped Block (hereafter named by its acronym SYDSB; Molnar & Tapponnier 1975; Tapponnier *et al.* 1990, 2001; Zhang 2013). The tranverse Lijiang-Xiaojinhe fault (F7 in Fig. 1), which divides the SYDSB into south and north portions (hereafter named by northern and southern SYDSB, respectively), and the Longmenshan fault (F8 in Fig. 1), form a part of the western boundary of the Yangtze Craton (Burchfiel *et al.* 1995; Zhang 2013).

Most of the late Permian Emeishan basalts exposed along the southeastern margin of Tibet are generally considered to be erosional remnants of voluminous mafic volcanic successions (Fig. 1) and are widely regarded to represent a large igneous province that was formed by a Permian plume (Xu *et al.* 2007). The thickness of the entire volcanic sequence in this province varies considerably, from over 5000 m in the west to a few hundred meters in the east (He *et al.* 2003). The province consists of dominant basaltic lavas and subordinate pyroclastic rocks. The Emeishan volcanic successions unconformably overlie the late middle Permian Maokou Limestone and are in turn covered by the uppermost Permian sediments in the east and west and by the upper Triassic or Jurassic sediments in the central part (He *et al.* 2003). Xu *et al.* (2007) identified at least seven lines of evidence that support a Permian mantle plume origin for the Emeishan large igneous province (ELIP). However, most of the evidence for this mantle plume has been derived from

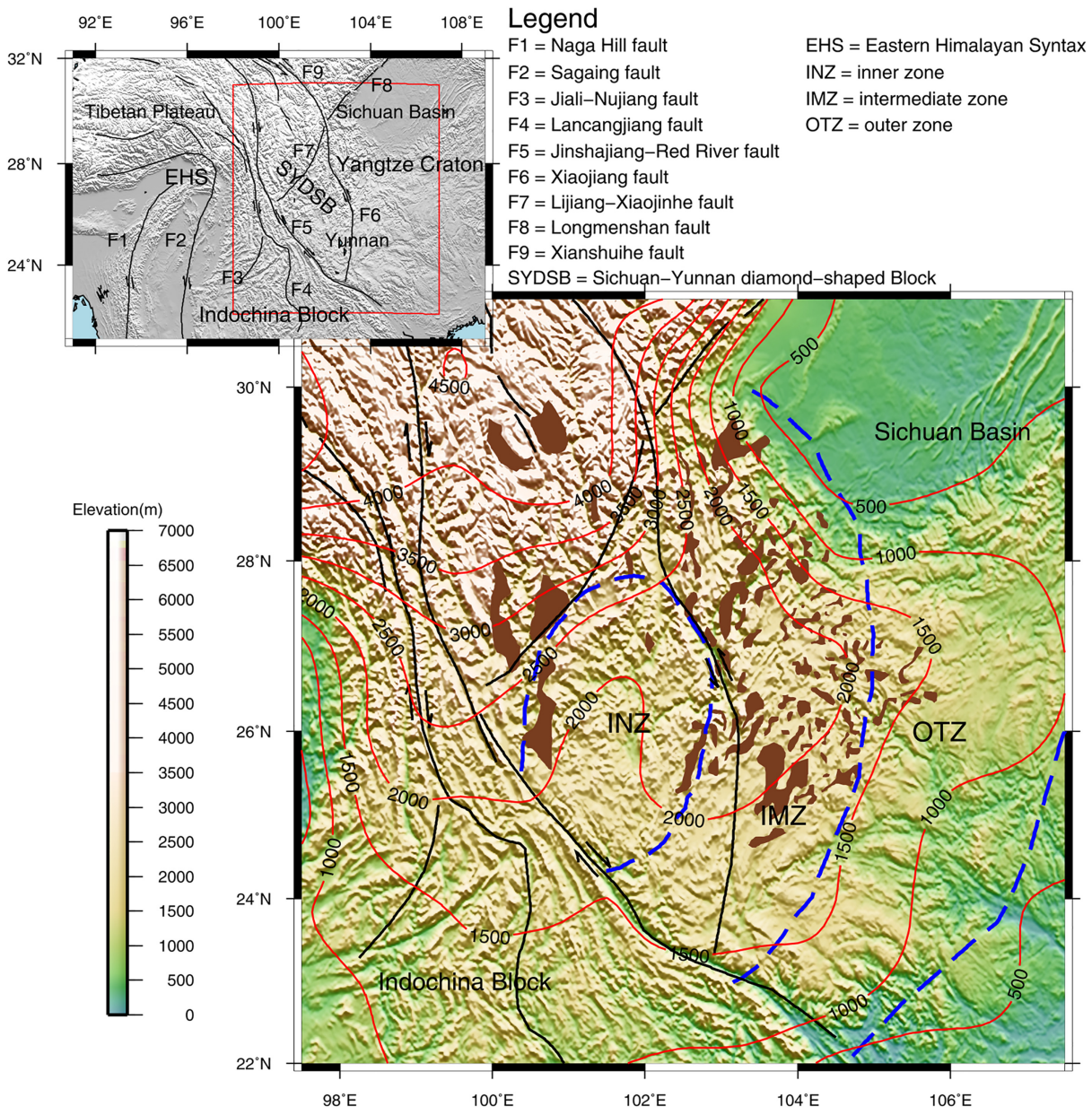

Figure 1. Tectonic situation of the ELIP and surrounding region across the southeastern margin of Tibet. The inset map in the upper-left-hand corner shows the main tectonic blocks and major faults (solid lines) in the region. The red rectangle encloses the study area. Shaded dark-brown areas indicate late Permian Emeishan basalts in the ELIP. Thick dashed blue lines mark the boundaries between the inner, intermediate, and outer zones of the ELIP. Thin black lines denote major faults. Red lines are isolines that represent the smoothed terrain elevation, with a colour scale of elevation shown to the left of the map.

geochemical, palaeomagnetic, geochronological and palaeontological studies, with limited evidence based on geophysical inferences. Previous studies (He *et al.* 2003, 2004, 2007; Xu *et al*. 2021) have indicated that the ELIP can be divided into inner (INZ), intermediate (IMZ), and outer (OTZ) zones on the basis of the extent of erosion of Maokou Limestone (Fig. 1). The INZ has a radius of *ca*. 200 km, where the the Maokou Limestone was strongly eroded and the pre-volcanic crustal uplift probably could exceed 1000 m (He *et al.* 2003; 2004, 2007; Xu *et al*. 2021). The thickness of the Maokou Limstone increases to 200–450 m in the INZ and to 250–600 m in the OTZ, suggesting a domal thinning of the strata in the ELIP (He *et al.* 2003). Most of the INZ lies within the southern portion of the Sichuan–Yunnan diamond-shaped block (SYDSB), and the INZ likely coincides with the centre of the postulated mantle plume (Xu *et al.* 2007). However, only scarce erosional remnants of the Emeishan basalts are exposed across the INZ (Fig. 1), and the INZ spans a large area; therefore, it is difficult to locate the plume head precisely. In fact, surface-wave tomography has imaged a 700-km-long northeast-trending zone of high shear-wave velocity and negative radial anisotropy around the INZ, which could be result of mafic-ultramafic, dyke-dominated magma storage system of the ELIP (Liu *et al.* 2021).

Thermomechanical models have predicted that the mantle plume postulated to have formed the ELIP should have generated a typical domal crust–mantle structure owing to strong plume–lithosphere interaction (Campbell & Griffiths 1990; Xu *et al.* 2007). This structure should show a gradual decrease in crustal thickness from the centre to the margins of the dome (Xu *et al.* 2007). The thermal effects of

a modern mantle plume are generally associated with geophysical responses to high lithospheric temperatures, such as seismic velocity and density anomalies within the lithosphere, which make the uppermost mantle an ideal target for seismological investigations. However, the ELIP is associated with an ancient plume that formed at *ca*. 260 Ma (Zhong *et al.* 2014), and the thermal structure associated with this Permian mantle plume activity may have decayed long ago. In addition, the lithosphere associated with the ELIP has migrated at least 3000 km to the north since its formation during the Permian (Huang *et al.* 2018). Fortunately, the continental crust (and possibly the lower lithosphere) can potentially preserve imprints of past dynamic evolution in the form of lithospheric composition and structure (Hawkesworth *et al.* 2013). Geophysical investigations may therefore be effective in identifying ancient mantle plumes by generating constraints on the composition and geometric structure of these ancient structures in the lithosphere, such as their crustal thickness and the depths/locations of intracrustal interfaces and the lithosphere–asthenosphere boundary (LAB).

Although geochemical evidence has been instrumental in inferring the origins of the ELIP (e.g. Xu *et al.* 2007), geophysical investigations have also been used to provide better constraints on the formation of the province. The observed positive residual gravity and corresponding high density across the ELIP have been attributed to large-scale mafic/ultramafic magmatic intrusions associated with a Permian plume eruption (Deng *et al.* 2014). The depth-migrated profile of calculated compressional-wave (*P* wave) receiver functions (PRFs) from a passive seismic profile across the ELIP has been interpreted as showing a 15–20-km-thick mafic layer that extends laterally for 150–180 km along the base of the crust in the INZ (Chen *et al.* 2015). Chen *et al.* (2015) attributed such a mafic layer to magmatic underplating at the base of the crust and intraplating within the upper crust. However, these inferences were based largely on a linear (2-D) profile. Wang *et al.* (2017) used calculated PRFs from 141 permanent stations and 785 temporary stations in the southeastern margin of Tibet to obtain values of crustal Poisson's ratio and thickness across that region. Although these results have provided reliable constraints on the geometry of the Moho along the southeastern margin of Tibet, the origin of the ELIP was not the focus of the previous studies. Reliable evidence for the existence of a Permian mantle plume is still lacking due to the absence of dense geophysical observations, with most of the evidence for the lithospheric structure of the ELIP having been based on geological and geochemical studies (e.g. Xu *et al.* 2007).

Here we calculate PRFs and shear wave receiver functions (SRFs)—two useful tools for exploring the crust and upper mantle structures—for the study area (Fig. 1). We also use data from a suite of geophysical methods to obtain a self-consistent 3-D model of the lithosphere of the ELIP and surrounding region and provide new insights into the origins of the ELIP. Our results provide a better understanding of the structure of the lithosphere beneath the ELIP and surrounding region, especially the structure of the lithospheric mantle.

2 DATA AND METHODS

One permanent and two temporary seismic arrays deployed across the southeastern margin of Tibet provided the original 3-component seismic-waveform data used in this study (Fig. 2a). The permanent seismic array has 118 permanent stations belonging to the China Regional Seismic Network and has been installed since 2008 (Fig. 2a). We selected numerous teleseismic events that occurred during the years 2010–2017: 114 $M_s \geq 6.8$ earthquakes at epicentral distances of 60–165° (Fig. 2b) to extract SRFs and 379 $M_s \geq 6.5$ earthquakes at epicentral distances of 30–95° (Fig. 2c) to isolate PRFs. The other seismic data sources used were the western Sichuan array, with 288 broad-band stations with a spacing of 10–30 km that were deployed during 2007–2009, and the ChinArray project with 350 broad-band stations with a spacing of ∼35 km that were in operation during 2011–2014. Each of the stations in these two temporary seismic arrays was equipped with either a CMG-3ESPC or CMG-40 seismometer and a REFTEK-130 recorder. We selected 259 earthquakes with magnitude $M_s \geq 5.4$ recorded by the first temporary array at epicentral distances of 30–95° (Fig. 2d), and 350 events equally with magnitude $M_s \geq 5.4$ that were recorded by the second temporary array within the same epicentral distance range (Fig. 2e).

PRFs can be obtained via a deconvolution algorithm to remove the source and path effects, which isolates the *P*-to-*S* converted waves from the *P*-wave coda that are generated at seismic discontinuities (e.g. Langston 1979; Ammon 1991; Zhu & Kanamori 2000). After a visual inspection of the three-component seismograms, we rotated all seismic traces from the ZNE coordinate system to the LQT ray-based coordinate system, then deconvolved the *L* component from the *Q* component in the time domain (Ligorria & Ammon 1999). To eliminate noise and obtain high signal-to-noise ratio receiver functions, we applied a low-pass Gaussian filter with a controlled-bandwidth parameter of $\alpha = 2.5$ to isolate PRFs (Langston 1979; Peng *et al.* 2019). Finally, we used common conversion point (CCP) stacking (Dueker & Sheehan 1998) to construct seismic profiles from the PRFs in the time domain, and a back-projection technique (Yuan *et al.* 1997) to construct a migrated image of the PRFs in the depth domain.

SRFs can isolate the *S*-to-*P* converted energy from the direct *S* arrivals (Yuan *et al.* 2006), and they possess a potential advantage over PRFs because the converted *P*-wave energy travels more quickly than the incoming *S*-wave energy, such that SRFs are relatively free of contaminated energy owing to first-order multiples. SRFs are therefore highly suitable for exploring the LAB and other upper-mantle low-velocity zones (e.g. Yuan *et al.* 2006; Li *et al.* 2007). Similarly, we deconvolved the *Q* component from the *L* component and used a low-pass Gaussian filter with a controlled-bandwidth parameter of $\alpha = 1.0$ to isolate SRFs. The time axis of the SRFs was reversed, such that the converted phases at discontinuities in the crust and upper mantle appear after the direct *S* wave, to display the SRFs in the same way as the PRFs. We also reversed the amplitudes of the SRFs, meaning that negative amplitude indicates a negative velocity gradient with depth and vice versa. Finally, we followed the procedure developed by Dueker & Sheehan (1998) to shift the SRFs from the time domain to the depth domain for measuring the depth of the LAB beneath the seismic stations.

3 RESULTS

3.1. Moho and LAB depths from SRFs

Fig. 3(a) shows the stations that were used to extract SRFs. All of these waveforms calculated at different stations were shifted from the time domain to the depth domain using a model modified from the IASP91 model (Kennett & Engdahl 1991) based on the *H–k* stacking results (Wang *et al.* 2017) and after being stacked into a single trace to deduce the respective Moho and LAB depths. Fig. 3(a) shows four reference profiles (A–B, C–D, E–F and G–H) at different latitudes across the ELIP, and Figs 3(b)–(e) shows the

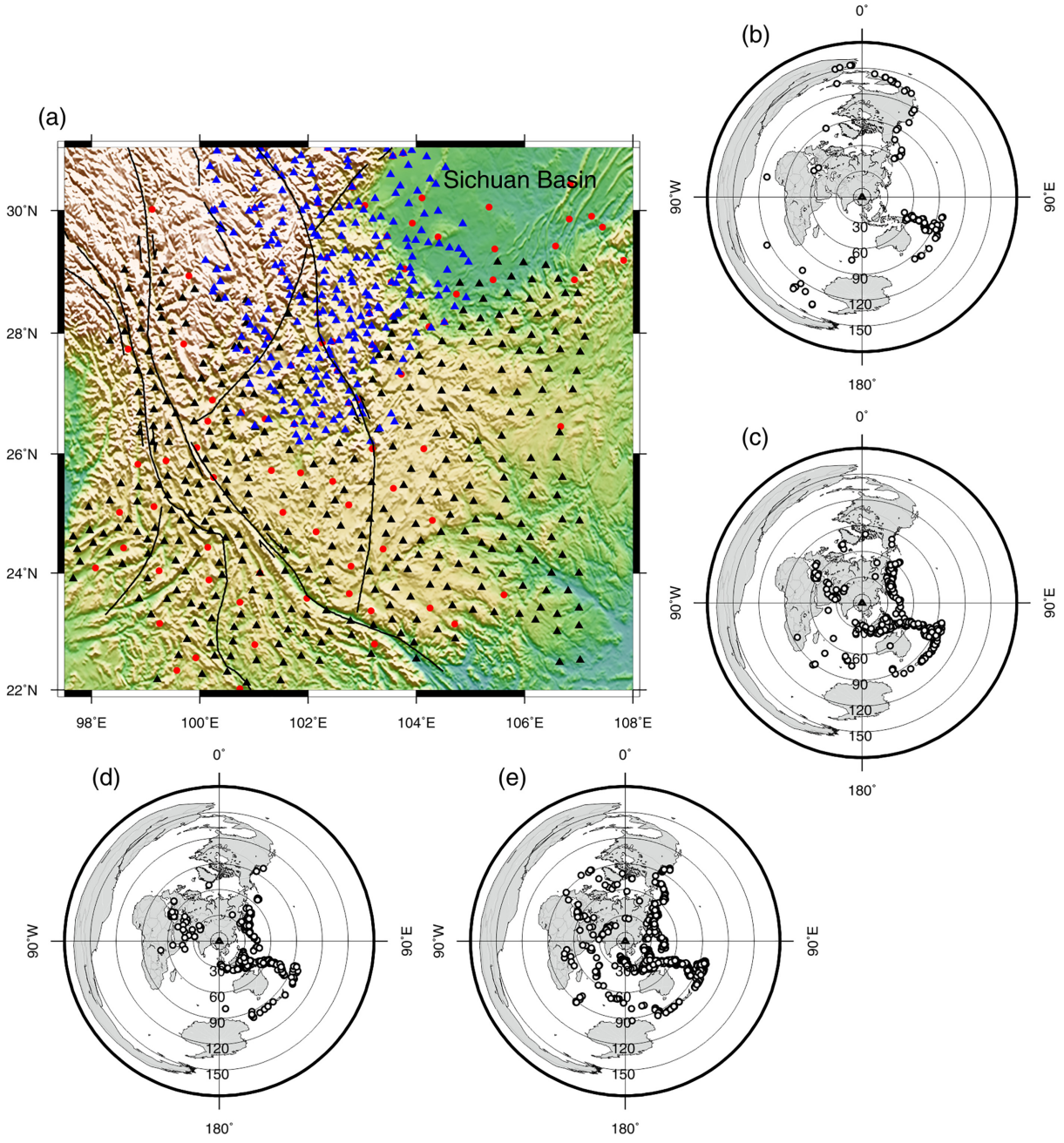

Figure 2. Broad-band seismic stations and earthquakes used in the study. (a) Locations of seismic stations. Red circles represent the permanent stations of the China Regional Seismic Network, and black and blue triangles indicate the temporary ChinArray and western Sichuan arrays, respectively. Black lines depict the main regional faults. (b) Earthquakes recorded at permanent stations at epicentral distances of 60–165° (small circles on a world map) and used to isolate the SRFs. (c) Earthquakes recorded at permanent stations at epicentral distances of 30–95° and used to isolate the PRFs. (d) Earthquakes recorded by the western Sichuan array (blue triangles) at epicentral distances of 30–95° and used to isolate the PRFs. (e) Earthquakes recorded by the ChinArray (black triangles) at epicentral distances of 30–95° and used to isolate the PRFs.

stacked SRFs along these profiles. The positive and negative *S*-to-*P* phases in the SRFs are highlighted by black and grey colours, and the maximum positive and negative amplitudes following incident *S* waves are interpreted as the converted phases at the Moho and LAB, respectively. It is worth noting that the slopes of the converted phases at the Moho that were recorded at some stations, such as PZH, HLI, SMK and PGE, are substantially broadened, which suggests that the Moho surface may be undulating. To check the coherence between individual SRFs and their stacked trace, as shown in Fig. S1 in the Supplementary Information, we plotted the individual and stacked SRFs for stations QIJ, XSB, YYU, PGE, DOC, PZH, HLI and SMK, which are installed in the northeastern INZ. Although the LAB is characterized by weaker seismic impedance than that of the Moho, it is noted that the *S*-to-*P* converted phases at the LAB for the individual SRFs exhibit better coherency than the *S*-to-*P* converted phases at the Moho (see Fig. S1), which suggests that the Moho may be more irregular than the LAB beneath the northeastern INZ of the ELIP.

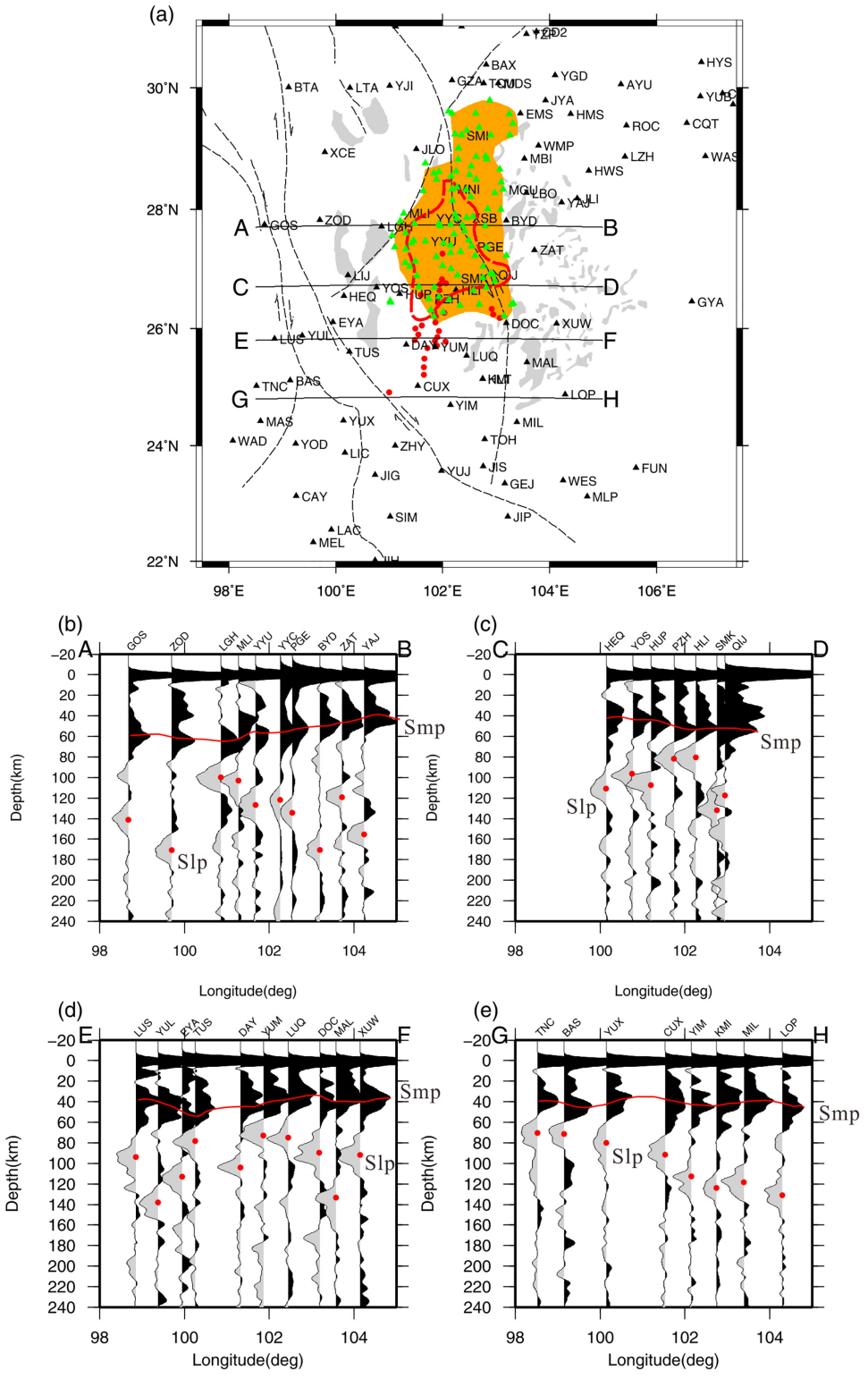

Figure 3. Stacked SRF profiles across the position of the head of the postulated Permian plume. (a) Permanent regional broad-band seismic stations (black triangles) and seismic profiles (A–B, C–D, E–F and G–H). Green triangles represent more than 90 stations that recorded either a double-lobe (or broadened) Pms phase or a positive converted phase at ∼5 s in addition to the Pms phase. Grey areas represent the Emeishan basalts, and the orange area marks the extent of the underplated layer. Red circles mark the positions of large V–Ti, Ni–Cu and Pt–Pd deposits. Dashed and solid lines denote the major faults (Fig. 1) and seismic profiles, respectively. The dashed red line depicts an area characterized by extremely mafic composition in the crust (Li *et al.* 2021). (b)–(e) Stacked SRF traces from the stations located within 45 km of a given profile. Station names are provided at the tops of the stacked traces. Black and grey wavelets represent positive and negative polarity phases, respectively. 'Smp' denotes the *S*-to-*P* converted phase at the Moho, and 'Slp' (red dots) represents the *S*-to-*P* converted phase at the LAB.

To draw contour maps of the Moho and LAB surfaces, we picked the Moho and LAB depths at each of the stations and then used GMT software (Wessel & Smith 1998) to perform a spline interpolation (Fig. 4). Values close to the margins of study area may not be reliable and were therefore not considered in the following analysis. The crustal thickness deduced from SRFs exhibits thickening towards the northwest and ranges from ∼33 km in southern Yunnan Province to ∼66 km across the Lijiang–Xiaojinhe fault (Fig. 4a). There is a marked increase in crustal thickness from ∼33 to ∼50 km around Panzhihua City, near station PZH (Fig. 4a), where the lithosphere is quite thin, with a thickness of ∼70 km (Fig. 4b). This thin lithosphere is located within the INZ of the ELIP (Fig. 4b) and belongs to the Yangtze Craton (Xu *et al.* 2020). The depth of the LAB is largely in the 130–160 km range within the Yangtze Craton, with the exception of the extremely thin lithosphere around Panzhihua City, and the thickest lithosphere (∼160 km) lies beneath the central Sichuan Basin (Fig. 4b). The Indochina block, which lies to the west of the Jinshajiang–Red River fault (Fig. 1) and is considered to constitute a series of extrusions from the eastern margin of Tibet that occurred during the early collision stage (Tapponnier *et al.* 2001), has a crustal thickness of ∼33 km and a LAB depth of only ∼90 km (Figs 4a and b). Due to the collection of a large number of teleseismic data, the current works provide a more reliable map of the lithospheric structure than our previous results (Hu *et al.* 2012).

3.2. CCP stacking profiles and depth-migrated PRF images

PRFs are sensitive to seismic discontinuities that generate *P*-to-*S* converted waves. These *P*-to-*S* converted arrivals depend on the ray path angle of incidence and the depth of the discontinuity (e.g. Langston 1979; Ammon 1991; Zhu & Kanamori 2000). To reveal the conversion signatures within the crust, the individual PRFs in the time domain were moveout corrected to a reference distance of 67° using the IASP91 model (Kennett & Engdahl 1991). We then applied the CCP stacking scheme of Dueker & Sheehan (1998) to obtain PRF profiles along latitudes 28°N, 27°N and 26°N (Figs 5a–c). The seismic traces were stacked within moving bins measuring 0.40° wide and 0.25° long based on the locations of the piercing point at 40 km depth. The Moho discontinuity represents a major change in velocities, compositions and rheology, thus the Moho *P*-to-*S* converted wave (Pms) is often the largest signal following direct *P*. The Pms arrivals generally occur in the 5–8 s range along the three profiles, which suggests the existence of pronounced lateral variations in crustal thickness. The Pms phases within the central INZ of the ELIP (101–103°E) exhibit an obvious broadened wavelet that potentially possesses double-lobe features (Fig. 5a), with significant increases in the delay times of the Pms phases in the central INZ, which implies the existence of a thick crust. However, these features are not observed in the IMZ of the ELIP. Two other dominant signatures can be recognized within the crust, they will be interpreted as Conrad Discontinuity (CD, at ∼2.5–3 s), and the underplating interface (UI, at 4–5 s) in the following section. However, they are observed only locally other than along the entire profile.

We investigated the lateral variation in converted *Ps*/*P* energy by back-projecting the individual PRFs along their respective paths, dividing the depth section into small boxes, and stacking the back-projected data within the same box. We used the 1-D IASP91 reference earth model (Kennett & Engdahl 1991) to calculate the piercing points at certain depths during this operation. Each box spanned a 20 km × 45 km horizontal interval and a 1.5 km vertical interval. We searched for all of the depth-migrated PRFs that were located in a given box, following which the back-projected individual amplitudes of PRFs falling in one box were stacked into a single value, which represents the converted Ps/P energy at the position of the box. The three depth-migrated profiles across the INZ of the ELIP are shown in Figs 5(d)–(f). In these profiles, positive *P*-to-*S* phases that occur at a depth range of ∼40–65 km are interpreted as the Moho, and a gradual decrease in the depth of the Moho is observed from the INZ to the IMZ of the ELIP. The greatest depth of ∼65 km is located in the northern INZ. In addition, a significant positive converted phase signature also exists at a depth of 35–40 km beneath the central INZ of the ELIP.

To reduce the influence of crustal velocities on the time-to-depth conversion, we used the crustal thickness and average *Vp*/*Vs* ratios determined by the *H*–*k* stacking method (Wang *et al.* 2017) to modify the IASP91 model. To reduce the complexity for imaging, we created a 1-D velocity model with grid cells of 1° × 1° and built the depth-migrated images in the grid cells, following which the images in each grid cell were combined into a single profile. As shown in Figs 6(a)–(c), the first-order patterns of the Moho topography in the profiles along 28°N, 27°N and 26°N are similar to those from the IASP91 model (Figs 5d–f), but the deepest Moho in the northern INZ is only ∼55 km, which is similar to those obtained by both the *H*–*k* stacking results (Wang *et al.* 2017) and the SRFs (see Fig. 4a). Nonetheless, the Moho topography pattern generated by the modified models does not exhibit significant variation in the southern ELIP, suggesting that the crustal structure may be close to that of the IASP91 model. To provide tight constraints on the positive converted phase signature at 35–40 km depth beneath the central INZ of the ELIP, we also created three other depth-migrated images along longitudes 101°E, 102°E and 103°E (Figs 6d–f). Except for the converted phases at the Moho, the pronounced positive converted phase at 35–40 km depth is most clearly revealed in the profile along 102°E, and its position is located in a longitude range of ∼101–103°E and a latitude range of ∼26–29°N (Figs 6 and S2).

3.3. *P*-to-*S* converted phases at an intracrustal interface

To verify our observations, we checked the individual and stacked PRFs recorded at each station and plotted the stacked PRFs at 93 stations located near the northeastern INZ of the ELIP (see the green triangles in Fig. 3a). All of these stacked traces are shown in Fig. 7. As a dominant feature, most of the *P*-to-*S* converted phases occur at 5–8 s and are represented by a positive double-lobe or a broadened wavelet. In addition to the wavelet, another *P*-to-*S* converted phase occurs at ∼5 s. For example, the stacked trace at station YYU (Fig. 7a) is a typical example with two positive converted phases: one at ∼5 s and another much more delayed at ∼8 s, corresponding to depths of ∼40 and ∼60 km, respectively. We checked the coherence between the individual PRFs and the stacked trace to test the reliability of these stacked traces, with Fig. S3 demonstrating that the individual PRFs are consistent with the stacked traces. Another feature is that these 93 stations are primarily distributed along a north–south-trending zone around the northeastern INZ (see orange area in Fig. 3a), whose position and lateral extent are similar to those of high shear wave velocity and negative radial anisotropy inferred from surface wave tomography (Liu *et al.* 2021).

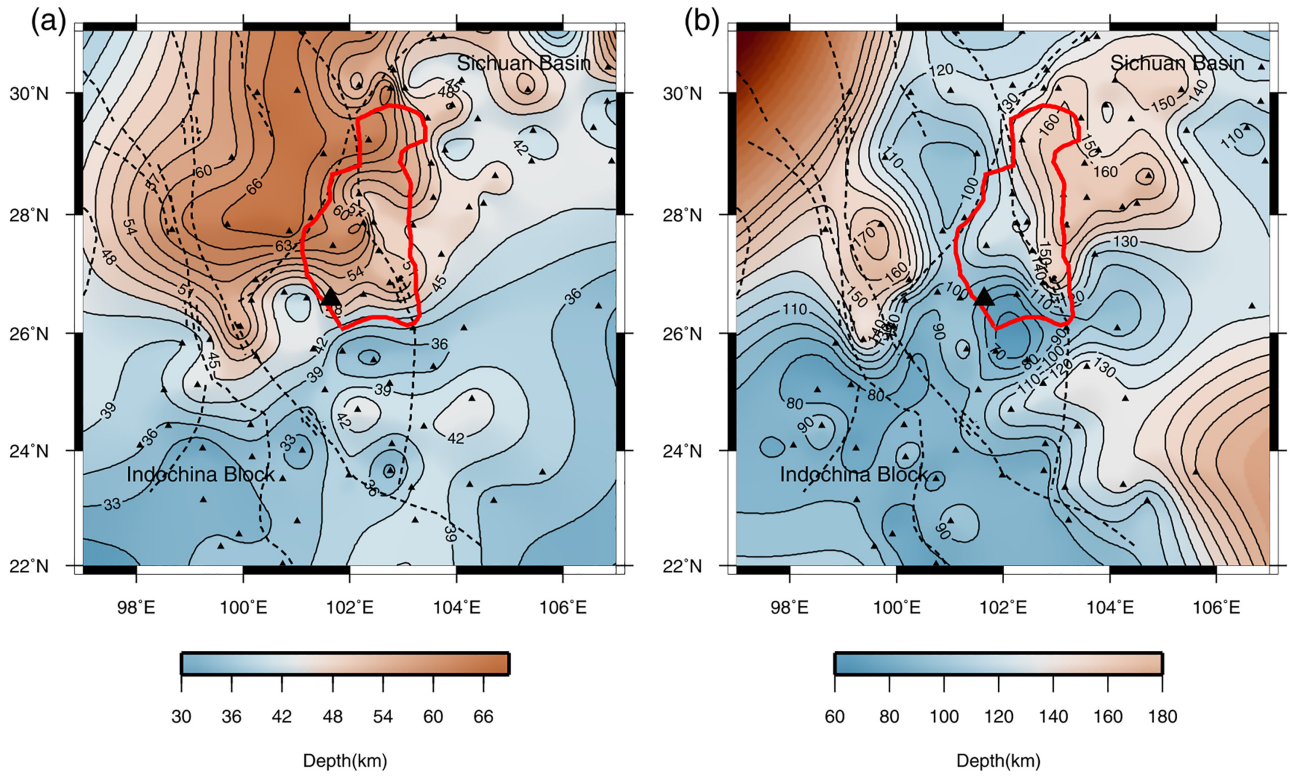

Figure 4. SRF-derived Moho (a) and LAB (b) contour maps (depth in km). The large black triangle marks the location of station PZH installed in Panzhihua City. Small triangles indicate permanent seismic stations, and dashed lines denote major faults. The wide red line marks the extent of the underplated layer (see orange area in Fig. 3a).

4 DISCUSSION

4.1. Interpretation of the LAB topography

The LAB is a first-order feature in many geodynamic models and plays an important role in mantle dynamics, although it is generally difficult to determine because of its locally weak seismic impedance. SRFs are suitable for imaging the mantle lithosphere as they theoretically allow a spatial resolution of ∼6 km vertically and ∼60 km horizontally, and synthetic tests have indicated spatial resolutions of ∼10 and ∼20 km for the LAB, respectively (Li *et al.* 2007). Our SRF results reveal a highly variable thickness of the lithosphere. The Indochina block, to the west of the Jinshajiang–Red River fault, is characterized by a predominantly shallow LAB (Fig. 4b) and thin crust (Fig. 4a), with LAB and Moho depths of 80–90 and 33–39 km, respectively. The Tengchong volcanic field (TVF) located in the northern block of Indochina (Fig. 8) comprises 68 volcanoes and 145 hot springs, with the last eruption having occurred in AD 1609, and it emits a high heat flow of ∼120 mW m^{-2} (Jiang *et al.* 2016). *P*-wave tomographic images have shown that there is an extremely low-velocity zone in the depth range of 100–400 km (Lei *et al.* 2009), which is reasonably consistent with our results. The thinning of the lithosphere and formation of the TVF are attributed to the hot mantle upwelling induced by the northeastward subduction of the Indian plate below Burma during the Cenozoic (Lei *et al.* 2009).

In contrast, to the east of the Jinshajiang–Red River fault, the depth of the LAB of the Yangtze Craton, which is bounded by the Longmenshan, Lijiang–Xiaojinhe and Jinshajiang–Red River faults to the west (Fig. 1), varies gradually from ∼70 km below central Yunnan Province to ∼160 km beneath the Sichuan Basin (Fig. 4b). The shallowest LAB (∼70 km) is observed in the central INZ of the ELIP. The lithosphere thickens abruptly from ∼100 to ∼160 km to the northwest of the Lijiang–Xiaojinhe fault in eastern Tibet. Unlike the Indochina block, the Yangtze Craton is an old, cold and rigid block (Xu *et al.* 2020) characterized by low heat flow (Fig. 8), except at the margin of the craton. Previous SKS shear wave splitting results indicate that there is a significant deformation transition zone near ∼26°N, suggesting that the deformation style of the upper mantle beneath the southern SYDSB differs substantially from that of the northern SYDSB (Wang *et al.* 2008). To the north of ∼26°N (corresponding to the plateau region north of the Lijiang–Xiaojinhe fault; Fig. 1), the appreciable deformation of the lithosphere (Fig. 4) can be related to the Indian–Eurasian continental collision, with the lithospheric thickening being attributed to obstruction of the lithospheric-scale escape flow from eastern Tibet by the rigid Yangtze Craton (Zhang *et al.* 2010). However, the shallowest LAB observed at ∼70 km depth in the central INZ of the ELIP cannot be explained by the India–Eurasia collision because of the aforementioned deformation transition zone near ∼26°N and the absence of an extremely low-velocity zone in the upper mantle beneath the southern SYDSB (Lei *et al.* 2009). In Section 4.4, we investigate the thinning of the lithosphere in the central INZ of the ELIP.

4.2. Seismic signature in the lithosphere

Beneath the INZ of the ELIP, the crust is characterized by high *Vp*/*Vs* ratios (Chen *et al.* 2015), high seismic wave velocities (Xu *et al.* 2015), and 15–20 km thickening (Chen *et al.* 2015; Xu *et al.* 2015). For determining crustal thickness, PRFs have an advantage

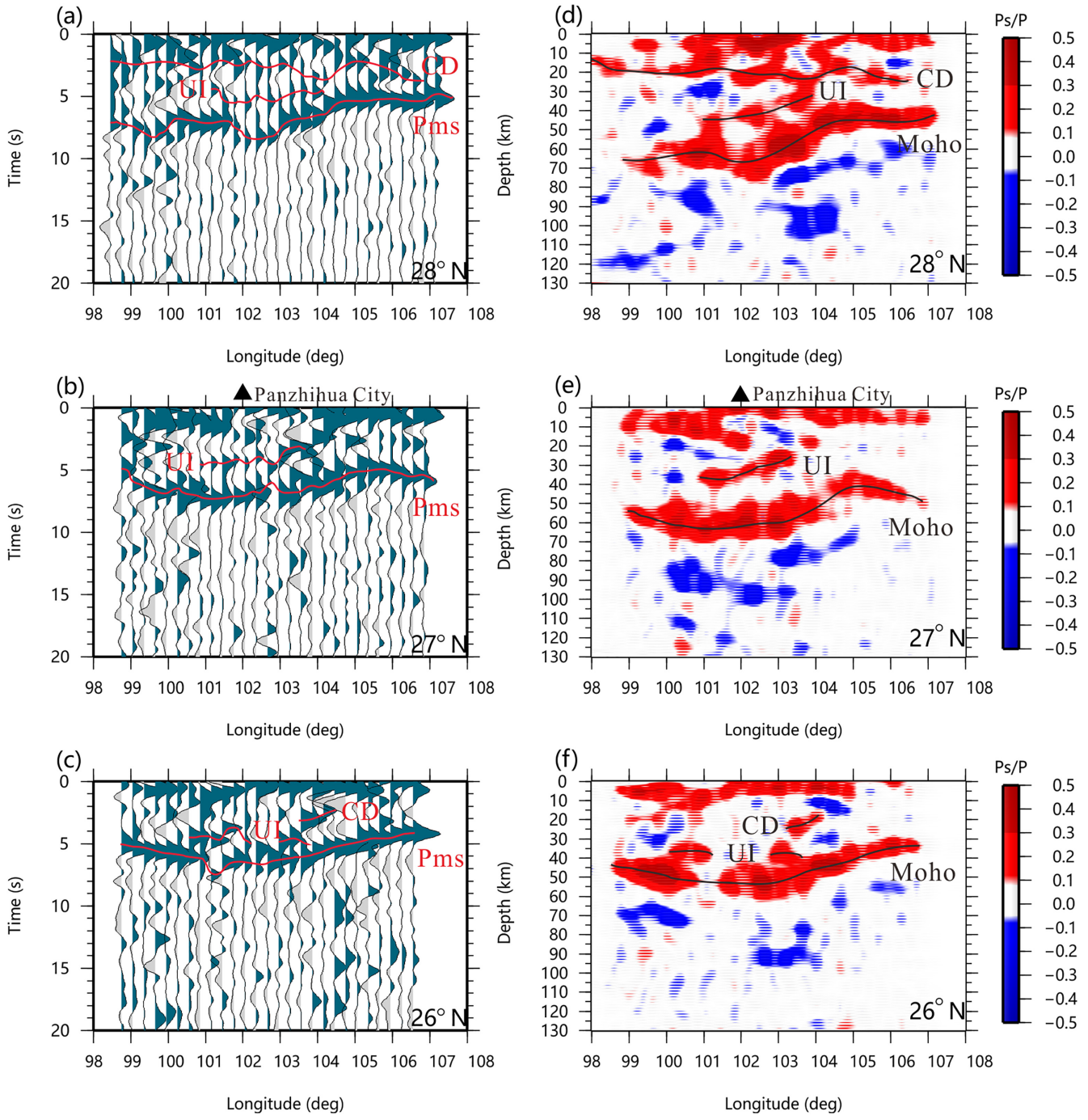

Figure 5. (a)–(c) CCP stacking profiles of the PRFs along (a) 28°N, (b) 27°N and (c) 26°N. Profiles were obtained by stacking the traces in the time domain that fell within moving bins measuring 0.40° wide and 0.25° long based on the locations of the piercing points at 40 km depth. 'Pms' denotes the *P*-to-*S* converted phases at the Moho. (d)–(f) PRF depth-migrated profiles of crustal structure based on the IASP91model (Kennett & Engdahl 1991) along (a) 28°N, (b) 27°N and (c) 26°N. UI, underplating interface; CD, Conrad discontinuity.

over SRFs in that they do not need a reference Earth model to calculate crustal depth. Wang *et al.* (2017) used the *H–k* stacking algorithm (Zhu & Kanamori 2000) to obtain values of crustal thickness and Poisson's ratio (see Fig. 9) from PRFs recorded at the above-mentioned three arrays. Their results revealed that the crustal thickness decreases from ∼60 km in the northern SYDSB to ∼30 km in southern Yunnan. The pattern of Moho topography deduced from PRFs (Fig. 9a) is generally consistent with that given by SRFs (Fig. 4a), with the largest discrepancy of ∼6 km being located in the northern SYDSB, where the crustal thickness is ∼60 km. In addition to a larger dominant period in the SRFs compared with the PRFs, in the case of a deep conversion discontinuity, this discrepancy may be due to the fact that SRFs sample a broader area than PRFs at the same focal distance, so the converted phases generated by a laterally heterogeneous structure could contaminate the converted phases at the Moho and LAB. However, our Moho topography for the INZ is very similar to that obtained by Wang *et al.* (2017), with one notable feature of our results being

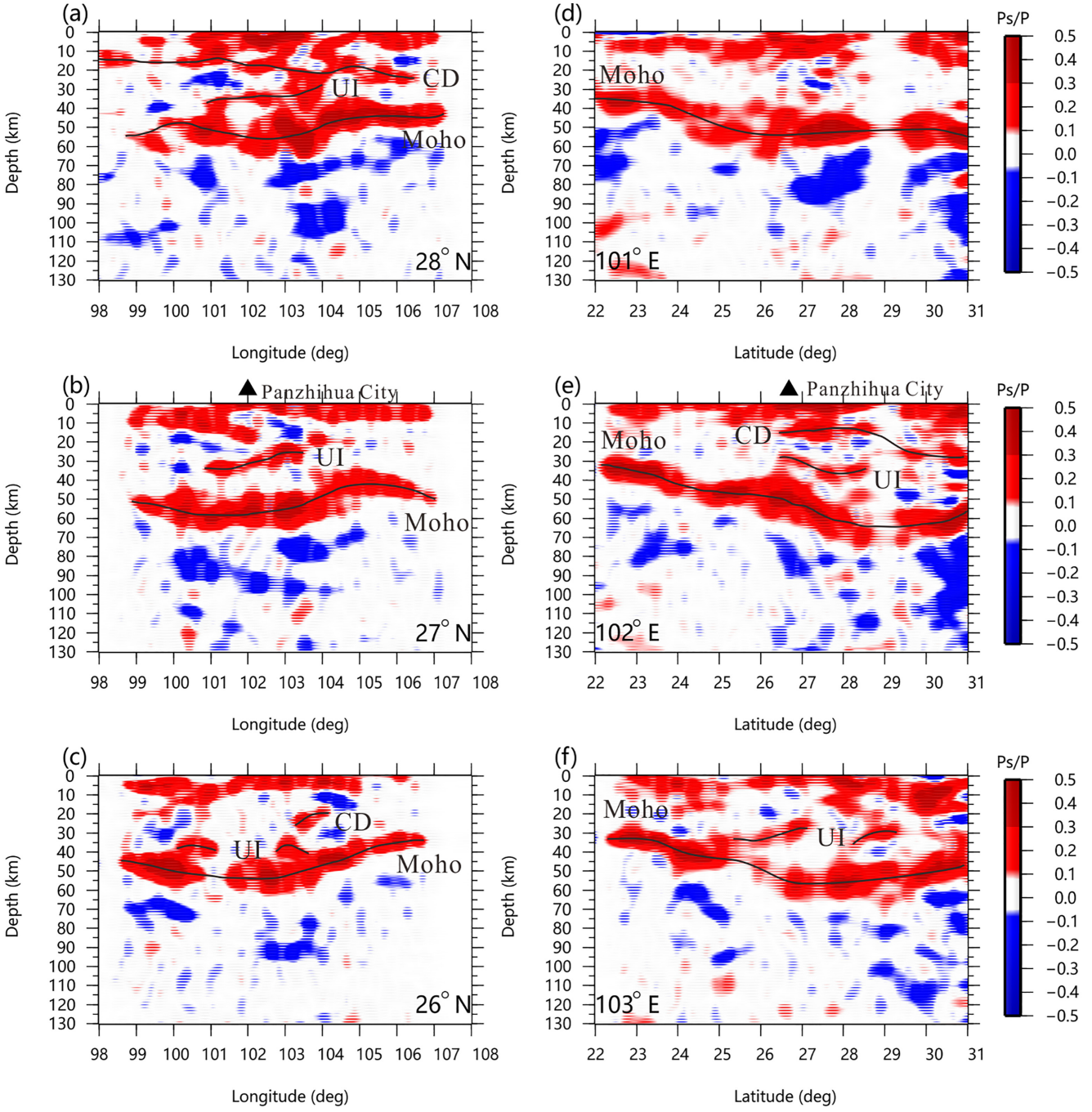

Figure 6. (a)–(c) PRF depth-migrated profiles of the crustal structure using a serials of 1-D velocity model with a grid cell size of 1° × 1° along (a) 28°N, (b) 27°N and (c) 26°N. (d)–(f) PRF depth-migrated profiles of the crustal structure using a serials of 1-D velocity model with a grid cell size of 1° × 1° along (d) 101°E, (e) 102°E and (f) 103°N. These 1-D reference models are modified from the IASP91model (Kennett & Engdahl 1991) based on the *Vp*/*Vs* and crustal thickness obtained by *H*–*k* stacking results (Wang *et al.* 2017). After building the depth-migrated image in each grid cell using the 1-D model, the images were combined into one profile. It is noted that the Moho obtained by these models along the 28°N profile is clearly shallower than that obtained by the IASP91 model. However, there is no clear difference along the 26°N and 27°N profiles.

the increase in crustal thickness from ∼42 km in the southern INZ to ∼57 km in the northeastern INZ. Fig. 9(b) shows that the crustal Poisson's ratio varies from 0.24 to 0.32, with high Poisson's ratio values of >0.28 occurring mainly along deep, large faults, such as the Xianshuihe, Lancangjiang, Jinshajiang–Red River and Longmenshan Faults. High bulk crustal Poisson's ratios beneath these faults (Fig. 9b) correspond to the locations of low-velocity zones, which may be related to the presence of partial melt (Wang *et al.* 2017). Here, we focus mainly on the high Poisson's ratio values of >0.28 around the northeastern INZ, which is characterized by a thick underplated layer along the base of the crust, as explained in the Section 4.3 (also see the area marked by the wide red line in Fig. 9). Previous studies (e.g. Zandt & Ammon 1995) have demonstrated that the lower crust must have a value of Poisson's ratio

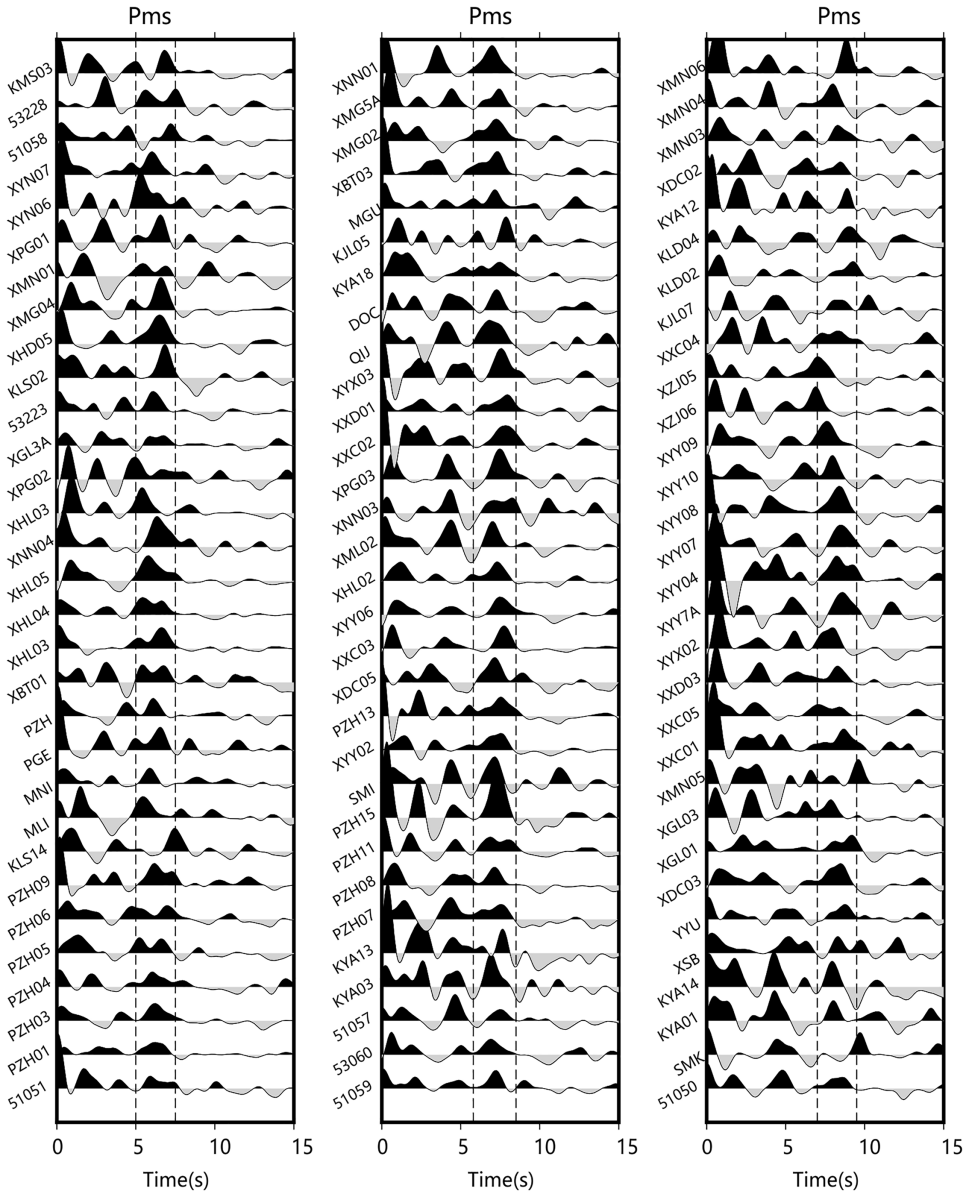

Figure 7. Stacked PRF traces at 93 stations (identified next to each trace on the left-hand side of each plot) located near the INZ and its surroundings (green triangles in Fig. 3a). All of these stations show either a double-lobe (or broadened) Pms phase or a positive converted phase at ∼5 s in addition to the Pms phase. 'Pms' denotes the *P*-to-*S* converted wave at the Moho.

of ∼0.30 if the bulk value of the entire crust is higher than 0.28. This range of Poisson's ratio and high *Vp* for the lower crust may reflect a mafic composition or the presence of water or another volatile component under high pore pressure. High pore pressure also decreases the velocity of both *P* and *S* waves substantially. The observed high *Vp* (Xu *et al.* 2015) and high Poisson's ratio (Wang *et al.* 2017) of cratonic lower crust strongly suggest a mafic composition of the northeastern INZ rather than other factors. It is noted that the Sichuan Basin is generally regarded as the core of the Yangtze Craton, and the high Poisson's ratio of >0.28 within its crust is attributed primarily to a thick sedimentary layer of ∼10 km thickness rather than a mafic composition (Wang *et al.* 2017).

The Pms delay times provide tight constraints on the Moho depth, as the wavelet and polarity of this converted phase provide information on the velocity contrast that generates the signal. A positive polarity generally indicates a positive velocity gradient, and vice versa. Our results demonstrate that two positive polarities are recognizable in the stacked PRFs both in the time domain (Figs 5a–c) and in the migrated images in the depth domain (Fig. 6). The two observed phases occur at ∼5 and ∼8 s in the central INZ, with corresponding depths of ∼40 and ∼55 km, respectively. We interpret that the deepest converted phase is Pms on the basis of its coherence across the CCP profiles (Figs 5a–c) and results of a previous study (Chen *et al.* 2015). The crustal thickness in the ELIP obtained from depth-migrated PRFs (Figs 6 and S2) approximately matches the *H–k* stacking results (Fig. 9a). Despite a reference earth model being required to produce depth-migrated PRF images, this match shows the Moho discontinuity with a high degree of reliability and that this modification to the IASP91 model using *H–k* results can be used to image crustal structure.

The CD is marked by the continuous positive amplitudes at ∼2.5–3.0 s (Figs 5a–c) or a depth of ∼20–25 km (Figs 6 and S2). It appears

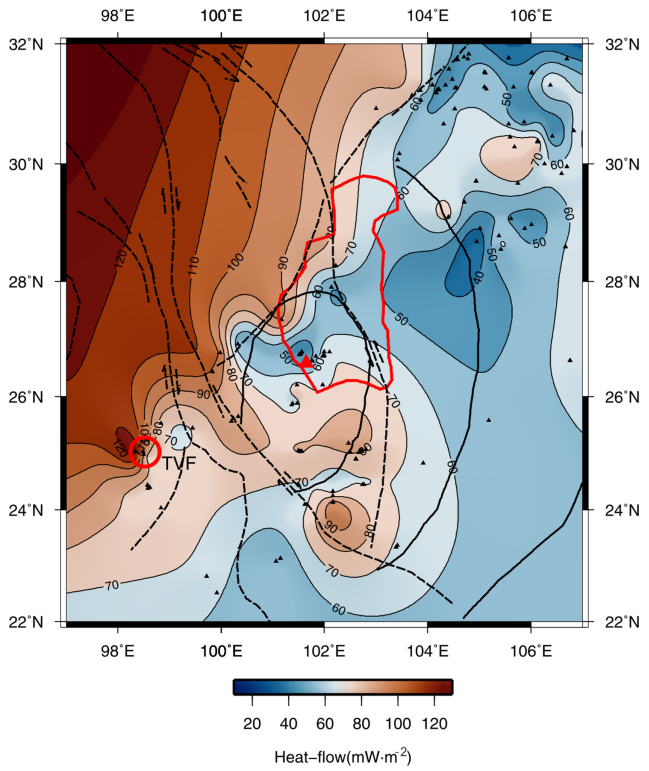

Figure 8. Heat-flow contour map (modified from Jiang *et al.* 2016). Black triangles denote measurement sites. The provided values are in mW m^{-2}. The circle denotes the Tengchong volcanic field (TVF), and dashed lines denote major faults (Fig. 1). Wide black lines mark the boundaries between the inner, intermediate, and outer zones of the ELIP. The wide red line marks the extent of the underplated layer (see orange area in Fig. 3a). The large red triangle marks the location of station PZH installed in Panzhihua City.

almost entirely throughout the profiles along 28°N and 29°N, and locally in the other profiles (Figs 6 and S2). The depth range (20–25 km) at which the CD appears corresponds to the base of the upper crust revealed by sounding profiles (e.g. Wang *et al.* 2007; Xu *et al.* 2015).

The positive converted phases observed at 4–5 s (Figs 5a–c) or ∼35–40 km depth (Figs 6 and S2) in the INZ are marked with the acronym 'UI' ('underplating interface') in the figures. The UI occurs 15–20 km above the Moho and covers an area of ∼150–200 km in the east–west direction and ∼400 km in the north–south direction (Figs 3a, 6 and S2). However, marked converted phases are observed along 101–103°E and 26–28°N, particularly along the profiles of 27–28°N and 102°E (Figs 6 and S2), but are seen only locally in the other profiles. Surface wave tomography images of the lithosphere under the ELIP confirm that a ∼15-km-thick high-velocity layer exists near the Moho in the INZ (Liu *et al.* 2021). The depth-migrated image of PRFs from a passive profile along ∼27°N suggests that a mafic layer of 15–20 km thickness and 150–180 km width exists at the base of the crust in the INZ (Chen *et al.* 2015). These results strongly support our observations and suggest that such a high-velocity layer existed near the Moho should be attributed to magmatic underplating at the base of the crust.

As shown in Fig. 7, the two *P*-to-*S* converted phases that occurred at ∼5 s (corresponding to ∼40 km depth) and ∼7 s (corresponding to ∼55 km depth) are confirmed by a previous linear passive seismic profile (Chen *et al.* 2015), although they are observed primarily around the northeastern INZ. The former converted phase could be generated at an intracrustal interface, or it could be the multiple converted phase PpPs at either crystalline basement or the CD. Synthetic experiments (Hazarika *et al.* 2012) have confirmed that a converted phase at crystalline basement could superpose on the direct *P* wave and broaden the direct *P* wave, and that the direct *P* wave is followed by a negative phase instead of a positive conversion phase. This experiment provides a priori knowledge for distinguishing converted phases at intracrustal interfaces from those at sediment. In comparison, the arrival time of the PpPs phase is ∼3.5 times that of the Ps phase (Yang *et al.* 2011). The *P*-to-*S* converted phase at the CD occurred at ∼2.5–3.0 s (Fig. 5), and its multiple converted phase PpPs should thus appear at ∼9–10 s. Therefore, we propose that the former phase (∼5 s) could not be the multiple converted phase PpPs at either crystalline basement or the CD, and interpret the former phase (∼5 s) as an intracrustal reflector and the latter (∼7 s) as the Moho on the basis of previous studies (Chen *et al.* 2015; Wang *et al.* 2017; Xu *et al.* 2020) and our own results from SRFs and PRFs (Figs 4a, 6 and S2).

These broadened and double-lobe Pms phases suggest that the Moho beneath the stations consists of either a sloped surface or possibly two discontinuities. However, these double-lobe phases would be combined into one wavelet with decreasing seismic wave frequency. The calculated SRFs from stations PZH, HLI, SMK and QIJ (Fig. 3a) possess *S*-to-*P* converted phases at the Moho that are also significantly broadened (Fig. 3c); this occurs because the SRFs cannot distinguish between the two interfaces on account of the lower resolution compared with the PRFs. The temporal variability of these converted phases suggests that the Moho is highly irregular around the northeastern INZ. Based on the results of previous studies (Chen *et al.* 2015; Wang *et al.* 2017; Liu *et al.* 2021), we interpreted the intracrustal reflector with high velocity as a cooled mafic underplated layer. Taking into consideration the spatial distribution of the 93 seismic stations that recorded either a double-lobe (or broadened) Pms phase or a positive converted phase at ∼5 s except for the Pms phase on the stacked PRFs (green triangles in Fig. 3a), as well as the inferred underplating in the depth-migrated PRF images (Figs 6 and S2), we depict a possible location of the underplated layer immediately below Panzhihua City and its surroundings (orange area in Fig. 3a). This underplated layer extends for 150–200 km in the E–W direction and ∼400 km in the N–S direction. Its position corresponds closely to that of a highly mafic crust (∼55.7 wt. per cent SiO_2; Li *et al.* 2021) in the northeastern INZ of the ELIP (Fig. 3a).

4.3. Gravity anomalies and lithospheric composition of the ELIP

Satellite gravity observations possess a key advantage over seismic observations in that they are not limited by the number and locations of recording stations. Measured Bouguer gravity anomaly is a summation of all density differences within the lithosphere with respect to the reference Earth model. The raw Bouguer gravity anomaly data were generated from the EGM2008 model (Pavlis *et al.* 2012). As shown in Fig. 10(a), the contour map of Bouguer anomalies indicates that the Bouguer anomaly varies from—200 in the central INZ of the ELIP to—240 mGal in the IMZ and is smaller than in other areas surrounding the INZ, suggesting the existence of either a shallower Moho or a higher density anomaly in the lithosphere beneath the central INZ than anywhere else. However, our observations and previous studies (e.g. Wang *et al.* 2017) did not support this inference on a shallow Moho in the central INZ. Deng *et al.* (2014)

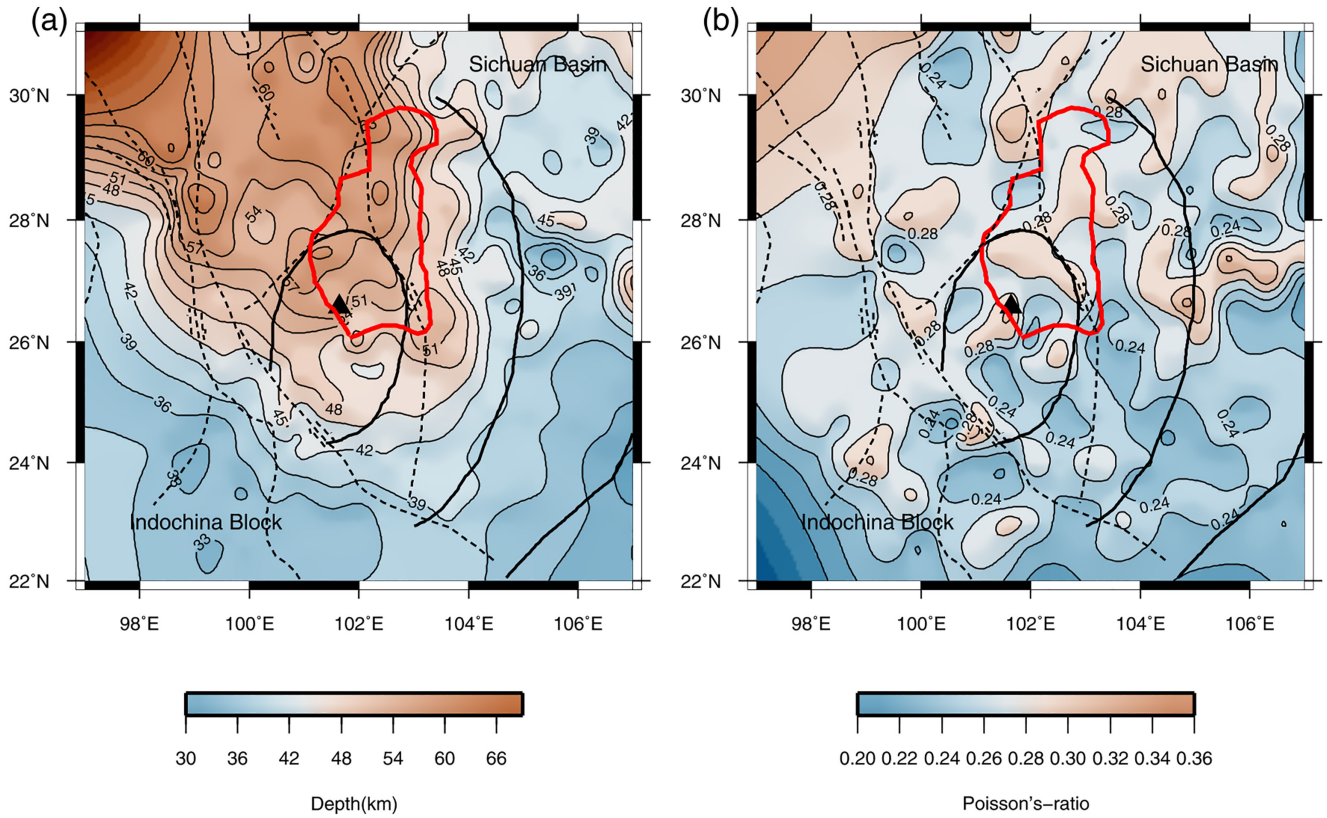

Figure 9. Contour maps of crustal thickness (a) and Poisson's ratio (b) obtained by Wang *et al.* (2017). The large black triangle marks the location of station PZH installed in Panzhihua City. Thin dashed black lines denote major faults (Fig. 1), and wide black lines mark the boundaries between the inner, intermediate, and outer zones of the ELIP. The wide red line marks the extent of the underplated layer (see orange area in Fig. 3a).

used a gravity-stripping method to remove the gravitational effects associated with sediments, crust and mantle lithosphere from the Bouguer gravity anomaly and obtained residual gravity anomalies. The consequent residual gravity reflects mainly the compositional density anomaly of the lithosphere with respect to the reference earth model. The results of Deng *et al.* (2014) showed the existence of a pronounced positive anomaly of +150 mGal in the INZ of the ELIP that decreases gradually with distance from the INZ (Fig. 10). An inverted density anomaly model shows that the INZ has a higher density anomaly (+0.06 g cm^{-3}) than the intermediate (+0.04 g cm^{-3}) and outer (+0.03 g cm^{-3}) zones, and that the affected region expands to ∼120 km depth in the INZ as it approaches the surface, whereas its influence decreases radially away from the INZ. A remarkable positive residual gravity anomaly exhibits close relationships with the spatial distribution of the inferred underplated layer in this study (see Fig. 10b), the low heat flow (Fig. 8), and the moderate–high values of Poisson's ratio (Fig. 9b). This high-density anomaly demonstrates the existence of large-scale magma intrusions into the lithosphere and crust along existing faults in the INZ, with the density of the rock mass consequently increasing gradually with time.

As well as the high Poisson's ratios in the northeastern INZ (Wang *et al.* 2017), an extremely mafic crust (∼55.7 wt. per cent SiO_2) has been found there (Li *et al.* 2021; see Fig. 3a), whose position and lateral extent are similar to those of the high-density anomaly (Fig. 10b), suggesting that the magma intrusion is composed of mafic materials. In addition to the formation of abundant basalts at the surface of the ELIP, the cooled mafic magma could have formed an underplating layer with high velocity near the Moho. In addition to the pronounced positive residual gravity anomaly providing an additional piece of independent evidence for the existence of mafic magma underplating in the northeastern INZ and its surrounding region, it also suggests that the lateral extents of ∼200 km in the E–W direction and ∼400 km in the N–S direction are similar to those inferred from the underplated layer depicted by the *P*-to-*S* converted phases at the studied intracrustal reflector (Fig. 10b), suggesting that the PRF analysis results are reliable.

4.4. Geodynamic implications

The INZ of the ELIP is currently located along the southeastern margin of Tibet, where the crust has undergone southeastward extension owing to continental collision between India and Eurasia during the Cenozoic (e.g. Clark & Royden 2000). The lower-crustal-flow model suggests that weaker lower-crustal materials have been flowing through the lower crust from central Tibet to Yunnan Province (Clark & Royden 2000; Royden *et al.* 2008), with crustal inflation occurring mainly within the lower crust. A continuous 15–20-km-thick mafic underplated layer is observed in the depth-migrated image in the region of 101–103°E and 26–29°N (Figs 6 and S2). Furthermore, the thickest portion of this underplated layer is centred beneath Panzhihua City and its surrounding region, which is recognized as a mineral-rich zone (particularly non-ferrous metals) and coincides with the thinnest lithosphere in the region (Figs 3a and 4b). In fact, the INZ of the ELIP is an important zone for V–Ti, Ni–Cu and Pt–Pd deposits in China (Fig. 3a). If this lower-crustal

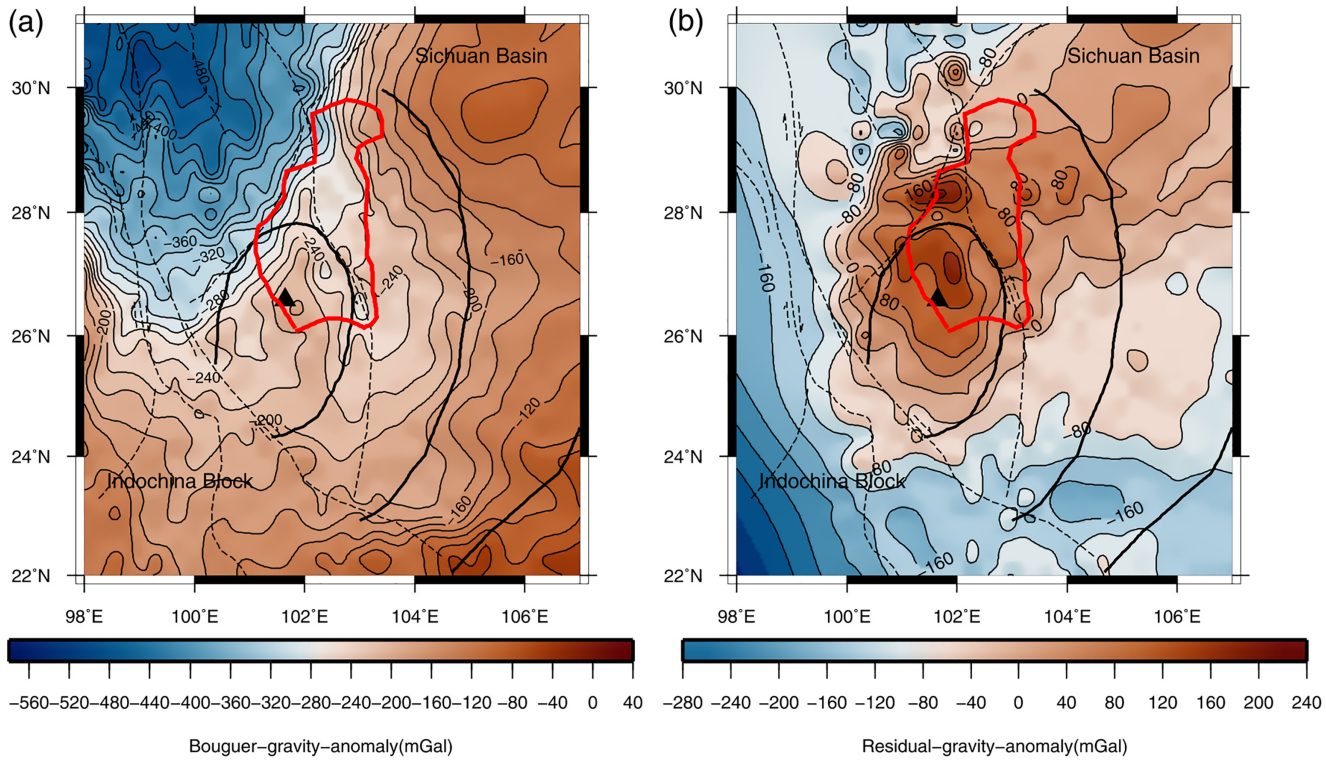

Figure 10. (a) Bouguer gravity map of the southeastern margin of Tibet (after Pavlis *et al.* 2012). (b) Residual gravity anomaly map obtained by removing the effects of sediment, crust and lithosphere from the Bouguer gravity (Deng *et al.* 2014). A pronounced positive anomaly (up to +150 mGal) extends over the inner, intermediate and outer zones of the ELIP. Thin dashed black lines denote major faults (Fig. 1), and wide dashed red lines mark the boundaries between the inner, intermediate and outer zones of the ELIP. The large black triangle marks the location of station PZH installed in Panzhihua City. The wide red line marks the extent of the underplated layer (see orange area in Fig. 3a).

flow has indeed occurred, and has penetrated the southeastern margin of Tibet, then alterations to the nature and geometry of the crust in the INZ of the ELIP would be unavoidable.

Our interpretation of magmatic underplating near the Moho owing to uplift of fossil mantle and the lack of modern hot mantle uplift is supported by low heat-flow measurements of only ∼50 mW m^{-2} in the central INZ (Fig. 8). Furthermore, this low heat flow in the central INZ implies that the observed uplift of the LAB is unlikely to be related to modern mantle dynamics. Recent palaeoaltimetry studies (Hoke *et al.* 2014; Li *et al.* 2015) have indicated that the plateau region north of the Lijiang–Xiaojinhe fault achieved its approximate current elevation by the late Eocene and have also suggested that the Lijiang–Xiaojinhe fault, which is the southwestern extension of the Longmenshan fault, was probably the boundary of the plateau during the late Eocene to early Miocene (Hoke *et al.* 2014; Li *et al.* 2015). Our results also indicate that the region near the Lijiang–Xiaojinhe fault, which is the northern border of the ELIP, is characterized by surface elevation (Fig. 1) and significant gradients of crustal thickness (Figs 4a and 9a) that could not be maintained if lower-crustal flow penetrated across the fault into the southeastern margin of Tibet (Bao *et al.* 2020). Crustal inflation has occurred in the lower crust beneath the northern region of the Lijiang–Xiaojinhe fault. Furthermore, the *S*-wave velocity structure from a joint inversion of Rayleigh wave dispersion, Rayleigh wave ZH spectral ratios and PRFs demonstrate that the local, mechanically strong crust beneath the INZ has obstructed southeastward crustal ductile flow and that thick crust–mantle transition zones exist beneath the INZ of the ELIP (Yang *et al.* 2020). These results also support our interpretation that the broadened or double-lobe Pms and broadend Smp phases are due to either a gradient Moho or an intracrustal reflector near the Moho. Therefore, we conclude that the observed magmatic underplating probably did not result from lower-crustal flow from central Tibet during the collision between India and Asia. Instead, we attribute this underplating to a large-scale fossil magmatic intrusion, such as a Permian mantle plume. Furthermore, if we assume crustal isostasy, then such large-scale magmatic underplating near the Moho would yield permanent kilometre-scale surface uplift. It is therefore suggested that the Emeishan basalts were strongly eroded via weathering and other subaerial processes as a response to this pronounced surface uplift, which may explain why there are almost no erosional remnants of Emeishan basalts within the INZ.

The southeastern margin of Tibet has undergone significant clockwise rotation around the EHS since 4 Ma owing to the lower-crustal flow injection and to deformation associated with the reversed motion of the Jinshajiang–Red River fault during the Miocene–Pliocene (Wang *et al.* 1998; Clark & Royden 2000; Wang & Burchfiel 2000; Clark *et al.* 2005). The portion of the INZ along the southern SYDSB could realistically have undergone southeastward extrusion based on this tectonic framework. However, Li *et al.* (2015) confirmed that this lateral extrusion was limited during the later stage of India–Eurasia collision. GPS velocity measurements have revealed southeastward movement of the SYDSB at ∼10 mm yr^{-1} (Zhang *et al.* 2004); accordingly, we estimate that no more than 40 km of displacement could have occurred since 4 Ma, even if the crust had been decoupled from the underlying mantle. Nonetheless, SKS splitting has confirmed that the crust is coherently coupled to the mantle north of ∼26°N (Wang *et al.* 2008). Although geological studies (e.g. Zhang 2013) have concluded that the total

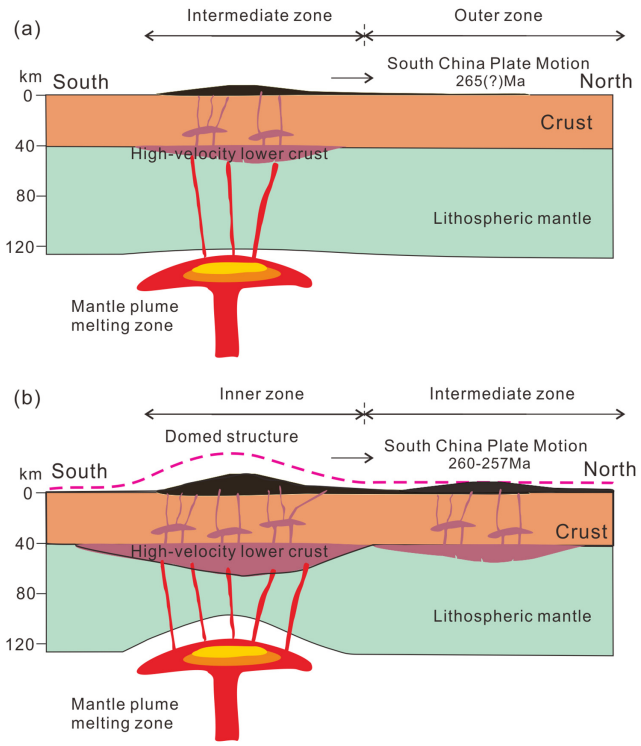

Figure 11. Schematic diagram of the origin of the Emeishan basalts, upwelling of hot mantle material and intrusion of melting material into the lithosphere and crust (modified from Xu *et al.* 2007). The cooled mantle materials not only strengthened the crust but also resulted in the formation of a high-velocity zone in the lower crust. (a) Upflow of mantle reached the bottom of the thick craton below the Sichuan Basin during the mid-Guadalupian (Shellnutt *et al.* 2012) and caused smooth and slow uplift of the surface. Melts began to form and partially penetrated the lithosphere. (b) As the South China plate drifted northward, the lithosphere under the present-day INZ moved just above the mantle upflow, and a major eruptive episode started at 260–257 Ma (Shellnutt *et al.* 2012). The upwelling hot mantle also removed the bottom of lithosphere by delamination, resulting in a thinned lithosphere.

left-lateral displacement on the Xianshuihe fault is 90–100 km, this displacement is too small to change the position of the magmatic underplating and its origin in the upper mantle.

Plume–lithosphere interactions may either destroy strong cratons by thermodynamic effects associated with the plume activity (e.g. Hu *et al*. 2018) or strengthen the mantle lithosphere by developing a craton-like mantle keel (Lee *et al*. 2011). Applying the plate reconstruction of Huang *et al.* (2018), we propose a schematic plume model to illustrate how the ELIP developed (Fig. 11). Assuming a stationary Emeishan hotspot, upflow of mantle reached the bottom of thick lithosphere but was unable to ascend much further until a thinner lithosphere had developed above the mantle upflow (Liu *et al.* 2021). However, as the South China Plate drifted northward, the thick craton beneath the Sichuan Basin lay directly above the mantle upflow during the mid-Guadalupian (Liu *et al.* 2021) and melts started to form, with the magma being able to penetrate partly into the lithosphere and solidify within the crust as underplated material and remain concealed beneath the large igneous province (Fig. 11a). At the same time, the magma intrusion into the crust caused slight uplift of the surface (Fig. 11a). This process may not only have added high-density material into the deep crust (Rudnick 1990) but may also have promoted additional crustal thickening through Moho deepening and/or uplift of the upper parts of the crust via physical (e.g. thermal density buoyancy) and chemical (e.g. melting, crystallization and differentiation) effects (Xu *et al.* 2007). Therefore, the underplating could be an indicator of plume activity, and the centre of the underplated area could coincide with the position of the head of the postulated plume.

As the South China block continued to move northward, a major volcanic episode occurred at 260–257 Ma near the Yangtze cratonic margin (Shellnutt *et al.* 2012), which corresponds to the present-day INZ (Fig. 11b). The upwelling hot mantle not only strengthened the crust by underplating but also removed the bottom of the lithosphere by delamination, resulting in a thinned lithosphere (Fig. 11b). In contrast to the Tarim Permian plume, in which plume–lithosphere interactions strengthened the mantle lithosphere by adding voluminous strong mafic rocks to the lithosphere and developing a craton-like mantle keel beneath the stable Tarim Basin (Xu *et al.* 2020), the northward drift of the South China block meant that the cooled magma in the upper mantle was unable to develop a craton-like mantle keel beneath the ELIP to maintain a thick lithosphere, which explains why the thinnest lithosphere (∼70 km) is observed in the central part of the INZ of the ELIP. However, as a result of the uplift of upper crust in the INZ, most of the Emeishan basalts on the surface were eroded, explaining the lack of erosional remnants of Emeishan basalts at the surface across the INZ.

We interpret the ∼400-km-long underplated layer from north to south as a likely plume head; specifically, the layer represents the Emeishan hotspot track. Furthermore, we infer that the scale of eruption may have been small during the early stage (the mid-Guadalupian) due to the small lateral extent of the northern part of the underplated layer. Variation in lithospheric thickness can affect the route of magma transport and storage and the location of major eruptions (Liu *et al.* 2021). The distinct lithospheric properties below Panzhihua City and its surroundings, including the high-density, thickened underplated layer and thinned lithosphere, suggest that the region of highly mafic crust in the northeastern INZ (the area marked by the dashed red line in Fig. 3a) likely coincides with the centre of the postulated mantle plume.

5 CONCLUSIONS

Our study used SRFs and PRFs to characterize the geometry and nature of the lithosphere underlying the ELIP in the southeastern margin of Tibet. We discovered a 15–20-km-thick mafic underplated layer that extends for 150–200 km in the E–W direction and ∼400 km in the N–S direction on along the base of the crust (Fig. 3a) in the northeastern INZ and its surrounding region, and identified a dome-shaped crust–mantle structure below the underplated layer. We propose that these features are unlikely to be related to the lower-crustal flow induced by India–Eurasia collision during the Cenozoic and instead represent Permian mantle plume activity. We interpret the underplated layer as the concealed Emeishan plume hotspot track and suggest that the head of the postulated mantle plume is centred approximately beneath Panzhihua City and its surroundings, where the lithosphere has thinned to ∼70 km, whereas the crust has thickened to ∼55 km. Voluminous mafic intrusions and underplating would have simultaneously strengthened the lower–middle crust. However, interaction between the Emeishan plume and the lithosphere, combined with the rapid northward movement of the South China block during plume activity, destroyed the Yangtze Craton in the plume region by removing the base of the lithosphere.

ACKNOWLEDGMENTS

The original seismic data used in this study were taken from the ChinArray–Himalaya Project. We thank the China Seismic Array Data Management Center (ChinArray DMC, doi:10.12001/ChinArray.Data, http://www.chinarraydmc.cn/) at the Institute of Geophysics, China Earthquake Administration, for providing the waveform data. We are grateful to Dr Xiao Yuan at GFZ for supplying his computer program for receiver function migration, and to Dr Yangfan Deng for providing gravity inversion results. We also thank Dr Weilai Wang for providing us with the thickness of the crust and the *Vp*/*Vs* ratio. Finally, we would like to thank two anonymous reviewers for their helpful comments and constructive suggestions that helped to better present this paper. In particular, we would like to express our sincere thanks to editor Dr Ian Bastow and assistant editor Louise Alexander for their helpful suggestions. This study was supported by the National Natural Science Foundation of China (grant 42174064).

DATA AVAILABILITY

The data underlying this paper were provided by the China Seismic Array Data Management Center (ChinArray DMC, doi:10.12001/ChinArray.Data, http://www.chinarraydmc.cn/) under licence/by permission. Data will be shared on request to the corresponding author with permission of the China Seismic Array Data Management Center.h1

CONFLICT OF INTEREST

The authors declare that they have no known competing financial interests or personal relationships that could have appeared to influence the work reported in this paper.

REFERENCES

Ammon, C. J., 1991. The isolation of receiver effects from teleseismic P waveforms. *Bull. seism. Soc. Am.,* **81,** 2504–2510.

Bao, X., Song, X., Eaton, D. W., Xu, Y. & Chen, H., 2020. Episodic lithospheric deformation in eastern Tibet inferred from seismic anisotropy. *Geophys. Res. Lett.,* **47,** e2019GL085721, doi:10.1029/2019GL085721.

Burchfiel, B.C., Chen, Z., Liu, Y. & Royden, L.H., 1995. Tectonics of the Longmen Shan and adjacent regions Central China, *Int. Geol. Rev.,* **37**(8), 661–735.

Campbell, I. H. & Griffiths, R. W., 1990. Implications of mantle plume structure for the evolution of flood basalts. *Earth planet. Sci. Lett.,* **99,** 79–93.

Chen, Y., Xu, Y., Xu, T., Si, Sh., Liang, X., Tian, X., Deng, Y., Chen, L., Wang, P., Xu, Y., Lan, H., Xiao, F., Li, W., Zhang, X., Yuan, X., Badal, J. & Teng, J., 2015. Magmatic underplating and crustal growth in the Emeishan Large Igneous Province, SW China, revealed by a passive seismic experiment. *Earth planet. Sci. Lett.,* **432,** 103–114.

Clark, M. K., House, M. A., Royden, L. H., Whipple, K. X., Burchfiel, B. C., Zhang, X. & Tang, W., 2005. Late Cenozoic uplift of southeastern Tibet. *Geology,* **33**(6), 525–528.

Clark, M. K. & Royden, L. H., 2000. Topographic ooze: building the eastern margin of Tibet by lower crustal flow. *Geology,* **28,** 703–706.

Deng, Y., Zhang, Z., Mooney, W., Badal, J., Fan, W. & Zhong, Q., 2014. Mantle origin of the Emeishan large igneous province (South China) from the analysis of residual gravity anomalies. *Lithos,* **204,** 4–13.

Dueker, K. G. & Sheehan, A. F., 1998. Mantle discontinuity structure beneath the Colorado Rocky Mountains and High Plains. *J. geophys. Res.,* **103,** 7153–7169.

Hawkesworth, C., Cawood, P. & Dhuime, B., 2013. Continental growth and the crustal record. *Tectonophysics,* **609,** 651–660.

Hazarika, D., Arora, B. R. & Bora, C., 2012. Crustal structure and deformation in the northeast India–Asia collision zone: constraints from receiver function analysis. *Geophys. J. Int.,* **188,** 737–749.

He, B., Xu, Y. G., Chung, S. L., Xiao, L. & Wang, Y. M., 2003. Sedimentary evidence for a rapid, kilometer-scale crustal doming prior to the eruption of the Emeishan flood basalts. *Earth planet. Sci. Lett.,* **213,** 391–405.

Hoke, G. D., Liu, Z. J., Hren, M. T., Wissink, G. K. & Garzione, C. N., 2014. Stable isotopes reveal high southeast Tibetan Plateau margin since the Paleogene. *Earth planet. Sci. Lett.,* **394,** 270–278.

Hu, J., Liu, L., Faccenda, M., Zhou, Q., Fischer, K. M., Marshak, S. & Lundstrom, C., 2018. Modification of the Western Gondwana craton by plume-lithosphere interaction. *Nat. Geosci.,* **11,** 203–210.

Hu, J., Yang, H., Xu, X., Wen, L. & Li, G., 2012. Lithospheric structure and crust-mantle decoupling in the southeast edge of the Tibetan Plateau. *Gondwana Res.,* **22,** 1060–1067.

Huang, B., Yan, Y., Piper, J. D., Zhang, D., Yi, Z., Yu, S. & Zhou, T., 2018. Paleomagnetic constraints on the paleogeography of the East Asian blocks during Late Paleozoic and Early Mesozoic times. *Earth Sci. Rev.,* **186,** 8–36.

Jiang, G. Z, Gao, P., Rao, S., Zhang, L. Y., Tang, X. Y., Huang, F., Zhao, P., Pang, Z. H., He, L. J., Hu, S. B. & Wang, J. Y., 2016. Compilation of heat flow data in the continental area of China(4th edition). *Chinese J. Geophys. (in Chinese),* **59**(8), 2892–2910.

Kennett, B. L. N. & Engdahl, E. R., 1991. Travel times for global earthquake location and phase identification. *Geophys. J. Int.,* **105,** 429–465.

Langston, C. A., 1979. Structure under Mount Rainer, Washington, inferred from teleseismic body wave. *J. geophys. Res.,* **84**(B9), 4749–4762.

Lee, C. T. A., Luffi, P. & Chin, E. J., 2011. Building and destroying continental mantle. *Annu. Rev. Earth planet. Sci.,* **39,** 59–90.

Lei, J., Zhao, D. & Su, Y., 2009. Insight into the origin of the Tengchong intraplate volcano and seismotectonics in southwest China from local and teleseismic data. *J. geophys. Res.,* **114**(B5), doi: 10.1029/2008JB005881.

Li, S., Currie, B. S., Rowley, D. B. & Ingalls, M., 2015. Cenozoic paleoaltimetry of the SE margin of the Tibetan Plateau: constraints on the tectonic evolution of the region. *Earth planet. Sci. Lett.,* **432,** 415–424.

Li, W., Chen, Y. & Xu, Y. G., 2021. Crustal SiO_2 content of the Emeishan large igneous province and its implications for magma volume and plumbing system. *Geochem. Geophys. Geosyst.,* **22,** e2021GC009783, doi:10.1029/2021GC009783.

Li, X., Yuan, X. & Kind, R., 2007. The lithosphere-asthenosphere boundary beneath the western United States. *Geophys. J. Int.,* **170,** 700–710.

Ligorria, J. P. & Ammon, C. J., 1999. Iterative deconvolution and receiver-function estimation. *Bull. seism. Soc. Am.,* **89,** 1395–1400.

Liu, Y., Li, L., van Wijk, J., Li, A. & Fu, Y. V., 2021. Surface-wave tomography of the Emeishan large igneous province (China): magma storage system, hidden hotspot track, and its impact on the Capitanian mass extinction. *Geology,* **49,** 1032–1037.

Molnar, P. & Tapponnier, P., 1975. Cenozoic tectonics of Asia: effects of a continental collision. *Science,* **189,** 419–426.

Pavlis, N. K., Holmes, S. A., Kenyon, S. C. & Factor, J. K., 2012. The development and evaluation of the Earth Gravitational Model 2008 (EGM2008). *J. geophys. Res.,* **117**(B4), doi:10.1029/2011JB008916.

Peng, H., Hu, J., Badal, J. & Yang, H., 2019. S-wave velocity images of the crust in the southeast margin of tibet revealed by receiver functions. *Pure appl. Geophys.,* **176,** 4223–4241.

Royden, L. H., Burchfiel, B. C. & Hilst, R. D., 2008. The geological evolution of the Tibetan Plateau. *Science,* **321,** 1054–1058.

Rudnick, R., 1990. Growing from below. *Nature,* **347,** 711–712.

Shellnutt, J. G., Denyszyn, S. W. & Mundil, R., 2012. Precise age determination of mafic and felsic intrusive rocks from the Permian Emeishan large igneous province (SW China). *Gondwana Res.,* **22,** 118–126.

Tapponnier, P., Lacassin, R., Leloup, P. H., Scharer, U., Zhong, D., Wu, H., Liu, X., Ji, S., Zhang, L. & Zhong, J., 1990. The Ailao Shan/Red River metamorphic belt: tertiary left-lateral shear between Indochina and South China. *Nature,* **343,** 431–437.

Tapponnier, P., Xu, Z., Roger, F., Meyer, B., Arnaud, N., Wittlinger, G. & Yang, J., 2001. Oblique stepwise rise and growth of the Tibet Plateau. *Science,* **294,** 1671–1677.

Wang, C. Y., Flesch, L. M., Silver, P. G., Chang, L. J. & Chan, W. W., 2008. Evidence for mechanically coupled lithosphere in central Asia and resulting implications. *Geology,* **36**(5), 363–366.

Wang, C. Y., Han, W. B., Wu, J. P., Lou, H. & Chan, W. W., 2007. Crustal structure beneath the eastern margin of the Tibetan Plateau and its tectonic implications. *J. geophys. Res.,* **112**(B7), doi:10.1029/2005JB003873.

Wang, E. C. & Burchfiel, B. C., 2000. Late Cenozoic to Holocene deformation in southwestern Sichuan and adjacent Yunnan, China, and its role in formation of the southeastern part of the Tibetan Plateau. *Bull. geol. Soc. Am.,* **112**(3), 413–423.

Wang, Erchi, Burchfiel, B. C. Royden, L. H. Chen, Liangzhong Chen, Jishen Li, Wenxin & Chen, Zhiliang 1998. *Late Cenozoic Xianshuihe-Xiaojiang, Red River, and Dali Fault Systems of Southwestern Sichuan and Central Yunnan, China,* **327** special paper, Geological Society of America, ISBN:9780813723273, doi:10.1130/SPE327.

Wang, W., Wu, J., Fang, L., Lai, G. & Cai, Y., 2017. Crustal thickness and Poisson's ratio in southwest China based on data from dense seismic arrays. *J. geophys. Res.,* **122,** 7219–7235.

Wessel, P. & Smith, W. H. F., 1998. New, improved version of generic mapping tools released. *EOS, Trans. Am. geophys. Un.,* **79**(47), 579–579.

Xu, M., Huang, Z., Wang, L., Xu, M., Zhang, Y., Mi, N., Yu, D. & Yuan, X., 2020. Sharp lateral Moho variations across the SE Tibetan margin and their implications for plateau growth. *J. geophys. Res.,* **125,** e2019JB018117, doi:10.1029/2019JB018117.

Xu, T., Zhang, Z., Liu, B., Chen, Y., Zhang, M., Tian, X., Xu, Y. & Teng, J., 2015. Crustal velocity structure in the Emeishan Large Igneous Province and evidence of the Permian mantle plume activity. *Sci. China Earth Sci.,* **58**(7), 1133–1147.

Xu, X., Zuza, A. V., Yin, A., Lin, X., Chen, H. & Yang, S., 2021. Permian plume-strengthened Tarim lithosphere controls the Cenozoic deformation pattern of the Himalayan-Tibetan orogeny. *Geology,* **49,** 96–100.

Xu, Y. G., He, B., Chung, S. L., Menzies, M. A. & Frey, F. A., 2004. Geologic, geochemical, and geophysical consequences of plume involvement in the Emeishan flood-basalt province. *Geology,* **32**(10), 917–920.

Xu, Y. G., He, B., Huang, X. L., Luo, Z. Y., Chung, S. L., Xiao, L., Zhu, D., Shao, H., Fan, W. M., Xu, J. F. & Wang, Y. J., 2007. Identification of mantle plumes in the Emeishan Large Igneous Province. *Episodes,* **30,** 32–42.

Yang, H., Hu, J., Li, G., Zhao, H. & Wen, L., 2011. Analysis of the crustal thickness and Poisson's ratio in eastern Tibet from teleseismic receiver functions. *Geophys. J. Int.,***186,** 1380–1388.

Yang, Y., Yao, H., Wu, H., Zhang, P. & Wang, M., 2020. A new crustal shear-velocity model in Southwest China from joint seismological inversion and its implications for regional crustal dynamics. *Geophys. J. Int.,* **220,** 1379–1393.

Yuan, X., Kind, R., Li, X. & Wang, R., 2006. The s receiver function: synthetics and data example. *Geophys. J. Int.,* **165,** 555–564.

Yuan, X., Ni, J., Kind, R., Mechie, J. & Sandvol, E., 1997. Lithospheric and upper mantle structure of southern Tibet from a seismological passive source experiment. *J. geophys. Res.,* **102,** 27 491–27 500.

Zandt, G. & Ammon, C.J., 1995. Continental-crust composition constrained by measurements of crustal Poisson ratio. *Nature,* **374**(9), 152–154.

Zhang, P. Z., 2013. A review on active tectonics and deep crustal processes of the Western Sichuan region, eastern margin of the Tibetan Plateau. *Tectonophysics,* **584,** 7–22.

Zhang, P. Z., Shen, Z., Wang, M. & Gan, W. 2004. Continuous deformation of the Tibetan Plateau from Global Positioning System data. *Geology,* **32,** 809–812.

Zhang, Z. J., Yuan, X. H., Chen, Y., Tian, X. B., Kind, R., Li, X. Q. & Teng, J., 2010. Seismic signature of the collision between the east Tibetan escape flow and the Sichuan Basin. *Earth planet. Sci. Lett.,* **292,** 254–264.

Zhong, Y. T., He, B., Mundil, R. & Xu, Y. G., 2014. CA-TIMS Zircon U-Pb dating of felsic ignimbrite from the Binchuan section: implications for the termination age of Emeishan large igneous province. *Lithos,* **204,** 14–19.

Zhu, L. & Kanamori, H., 2000. Moho depth variation in southern California from teleseismic receiver functions. *J. geophys. Res.,* **105**(B2), 2969–2980.

SUPPORTING INFORMATION

Supplementary data are available at *GJI* online.

Please note: Oxford University Press is not responsible for the content or functionality of any supporting materials supplied by the authors. Any queries (other than missing material) should be directed to the corresponding author for the paper.